Advanced Composite Materials
Publication details, including instructions for authors and subscription information:
http://www.tandfonline.com/loi/tacm20

Effect of Anisotropic Properties on Defect Detection by Pulse Phase Thermography

Masashi Ishikawa [a], Hiroshi Hatta [b], Yoshio Habuka [c], Sayaka Jinnai [c] & Shin Utsunomiya [d]

[a] The Graduate University for Advanced Studies (Sokendai), 3-1-1 Yoshinodai Chuo-ku, Sagamihara, Kanagawa 252-5210, Japan

[b] The Graduate University for Advanced Studies (Sokendai)/ Japan Aerospace Exploration Agency, 3-1-1 Yoshinodai Chuo-ku, Sagamihara, Kanagawa 252-5210, Japan

[c] Krautkramer Japan, Co., Ltd., 4th Floor Totojidosha Bldg. 5-13-3 Nishiikebukuro, Toshima-ku, Tokyo 171-0021, Japan

[d] Japan Aerospace Exploration Agency, 2-1-1 Sengen, Tsukuba, Ibaraki 305-8505, Japan

Version of record first published: 17 Jul 2012.

To cite this article: Masashi Ishikawa , Hiroshi Hatta , Yoshio Habuka , Sayaka Jinnai & Shin Utsunomiya (2012): Effect of Anisotropic Properties on Defect Detection by Pulse Phase Thermography, Advanced Composite Materials, 21:1, 67-78

To link to this article: http://dx.doi.org/10.1163/156855112X629513

///VSP///

Advanced Composite Materials 21 (2012) 67–78

ADVANCED COMPOSITE MATERIALS
brill.nl/acm

Effect of Anisotropic Properties on Defect Detection by Pulse Phase Thermography

Masashi Ishikawa [a,*], **Hiroshi Hatta** [b], **Yoshio Habuka** [c], **Sayaka Jinnai** [c] **and Shin Utsunomiya** [d]

[a] The Graduate University for Advanced Studies (Sokendai), 3-1-1 Yoshinodai Chuo-ku, Sagamihara, Kanagawa 252-5210, Japan

[b] The Graduate University for Advanced Studies (Sokendai)/Japan Aerospace Exploration Agency, 3-1-1 Yoshinodai Chuo-ku, Sagamihara, Kanagawa 252-5210, Japan

[c] Krautkramer Japan, Co., Ltd., 4th Floor Totojidosha Bldg. 5-13-3 Nishiikebukuro, Toshima-ku, Tokyo 171-0021, Japan

[d] Japan Aerospace Exploration Agency, 2-1-1 Sengen, Tsukuba, Ibaraki 305-8505, Japan

Received 22 October 2011; accepted 21 December 2011

Abstract

The influence of anisotropic thermal diffusivities on non-destructive testing of CFRP laminates using pulse phase thermography (PPT) was studied analytically. The results show that the optimum frequency for maximizing detectable depths of defects increases concomitantly with the increase in the ratio of the thermal diffusivities in the through-thickness direction to that in the in-plane direction (α'). Furthermore, the phase difference between sound and defective areas decreases significantly with decreased α'. These predicted tendencies were verified through experiments. Experimental results also demonstrated that defects of 10 mm in diameter can be detected up to around 5 mm depth in CFRP with lower α', but only to around 1 mm in CFRP with higher α'.

Keywords

Non-destructive testing, infrared thermography, CFRP, finite element analysis

1. Introduction

Infrared thermographic non-destructive testing (IR-NDT) is a non-contact method featuring shorter inspection time and covering a wider area than other NDT methods, such as ultrasonic techniques. Consequently, this method is expected to be utilized for inspection of composite materials such as carbon fiber reinforced polymer (CFRP) used in aerospace and automotive structures.

* To whom correspondence should be addressed. E-mail: ishikawa.masashi@ac.jaxa.jp
Edited by the JSCM

DOI:10.1163/156855112X629513

CFRPs have been inspected using pulse thermography (PT) [1–4] and lock-in thermography (LT) [4–9]. With PT, an object surface is heated instantaneously by flash lamps. Then, the surface temperature distribution after heating is monitored using an infrared camera. Defects inside the object are identified as a local temperature rise on the surface immediately above the defect, attributable to the disturbance of heat flow around the defect. In contrast, with LT, the testing object surface is heated periodically (e.g., sinusoidally). The surface temperature (T) after heating is correlated with input heating (q) as a function of elapsed time, and the phase delay between T and q is determined. Then, a phase image is constructed using the phase delay. In the phase image, the detectable depth of defects was found to be better than that obtainable using PT, with accompanying relief of the influence of non-uniform surface heating [9]. However, both methods present a disadvantage that their detectable defect depth is limited to a few millimeters. In CFRP laminates, the detectable depth is smaller than in isotropic materials because heat applied on the surface has difficulty in propagating in the through-thickness direction because of the laminates' much lower thermal diffusivity in the through-thickness direction than in the in-plane ones. Previous researchers have reported that the detectable depth of defects in CFRP was up to 3 mm using PT (defect diameter d of 10 mm) [3], and up to 2 mm using LT ($d = 6$ mm) [8].

Pulse phase thermography (PPT) is another procedure that combines the advantages of PT and LT. In PPT, the temperature–time data ($T(t)$) obtained using the same procedure as PT are transformed to phase–frequency data ($\phi(f)$) by the Fourier transform. Then, phase images are constructed from $\phi(f)$. In the phase images, the detectable defect depth is improved, and the influence of non-uniform heating is relieved, as with LT [10]. Additionally, the detectable defect depth is reportedly enhanced when using phase images in a low frequency range [11–13]. The present authors revealed the mechanism for those results through discussion based on analytical calculations, and the optimum frequencies for detection of defects were determined at various depths in polymethylmethacrylate (PMMA) [14].

Few papers have described application of PPT for detection of defects in CFRPs [15–17]. Because CFRPs possess anisotropic thermal diffusivity, detectable depth is expected to vary depending on their anisotropy. In this paper, the influence of thermal anisotropy on the phase data obtained by PPT is studied analytically. The optimum frequency to maximize detectable depth was obtained as a function of the ratio of thermal diffusivities in the in-plane direction to that in the through-thickness direction. In addition, PPT experiments for CFRPs of two types with different thermal anisotropies were conducted, and the experimentally obtained results were compared with the analytical results.

2. Pulse Phase Thermography

The PPT inspection procedure is presented in Fig. 1. As in the PT method, the object surface is heated using flash lamps, and the surface temperature after heating ($T(t)$)

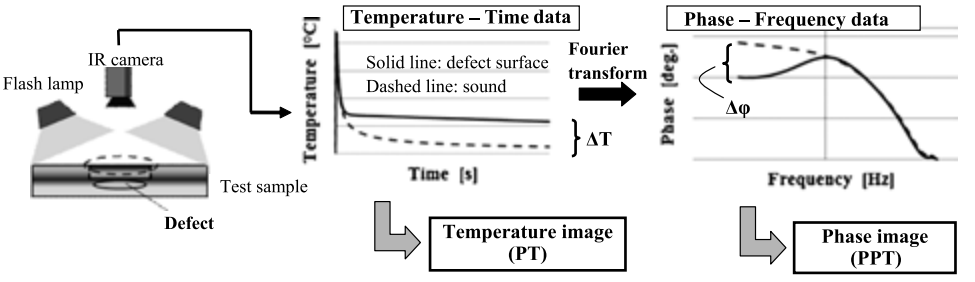

Figure 1. Inspection procedure and data processing adopted in the pulse phase thermography.

is monitored using an infrared camera. In PT, two-dimensional temperature images are constructed using $T(t)$, and interior defects are detected utilizing temperature difference between defective and non-defective area (ΔT) in the temperature images. On the other hand, in PPT, the discrete Fourier transformation is applied to $T(t)$, and phase data are calculated as a function of frequency ($\phi(f)$) using the equation below.

$$\phi(f) = \tan^{-1}\{I(f)/R(f)\}, \tag{1}$$

where f stands for the frequency, and $R(f)$ and $I(f)$ are the real and imaginary components obtained using the Fourier transform. Then, phase images for various frequencies are constructed using $\phi(f)$. In the phase images, interior defects appear as color contrast caused by the phase difference between defective and non-defective areas ($\Delta\phi$).

A calculable frequency range of $\phi(f)$ depends on the sampling frequency of the infrared camera (f_s) and number of data (n). The maximum and minimum frequencies (denoted respectively as f_{max} and f_{min}) are given as

$$f_{max} = f_s/2 \quad \text{and} \tag{2}$$

$$f_{min} = f_s/n. \tag{3}$$

Equation (3) shows that, to obtain $\phi(f)$ at a lower frequency, lower f_s and larger n are necessary. These conditions demand a long inspection time.

3. FEM Analyses

The effect of defect geometry and thermal anisotropy on PPT results was examined using axi-symmetric calculations based on the finite element method (FEM). For analyses, commercial FEM software ABAQUS 6.7 (Simulia; Dassault Systemes) was used.

3.1. FEM Models

Flat-bottomed defects were modeled as depicted in Fig. 2. The model is axisymmetric; defect depth h and defect diameter d were varied. Pulse heating with duration of 3 ms was assumed to be applied uniformly on the upper surface of the models,

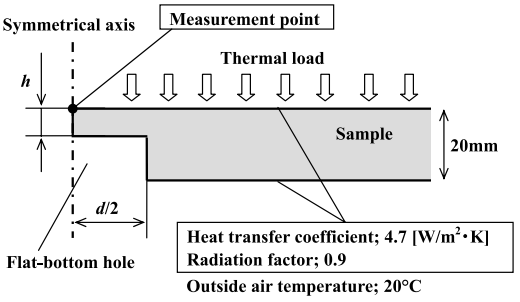

Figure 2. Axisymmetric model used in finite element calculations.

Table 1.
Thermal properties used in FEM calculations

	Sample 1	Sample 2	Sample 3	Sample 4	Sample 5
Density ρ (kg/m^3)			1536		
Specific heat capacity c (J/(kg · K))			865		
Thermal conductivity (W/(m · K))					
In-plane k_L	0.48	2	6.0	40	71.7
Out-of-plane k_T			0.48		
Thermal diffusivity (mm^2/s)					
In-plane α_L	0.36	1.51	4.5	30	54
Out-of-plane α_T			0.36		
$\alpha'(=\alpha_L/\alpha_T)$	1	4.2	12.5	83.3	150

where the environmental temperature was assumed as 20°C, and the heat-transfer coefficient and radiation factor at the upper and bottom boundaries of the model were set respectively to 4.7 W/m^2 K and 0.9 (these are estimated values used in previous studies [18]).

The phase-frequency data $\phi(f)$ at the surface point immediately above the defect center was calculated for the cases of $d = 5$, 10 and 20 mm and $h = 0.25$–5 mm. For comparison, the $\phi(f)$s for $h = 0.25$–5 mm and 20 mm, $d = \infty$ were calculated. The Fourier transformations were obtained by setting a sampling frequency f_s of 2 Hz, and data points n of 4096. Five different thermal properties presented in Table 1 (*Samples 1–5*) were used for analyses. As the table shows, calculations were performed with variance only of the thermal conductivity in in-plane direction (k_L) to study the influence of anisotropy of laminates, where Sample 1 simulates an isotropic material. Thermal diffusivities (α) given as $\alpha = k/(\rho c)$ (ρ is density and c specific heat) and the ratios of αs between the in-plane and out-of-plane direction ($\alpha' = \alpha_L/\alpha_T$) are also shown in Table 1.

3.2. Results

Figure 3 shows the phase difference between sound ($h = 20$ mm, $d = \infty$) and the defective ($h = 1$ mm, $d = 5$, 10, 20 mm) area for Sample 1 and Sample 2 ($\alpha' = 1$ and 4.2) as a function of frequency ($\Delta\phi(f)$). In this study, phase data calculated from the conditions of $h = 20$ mm, $d = \infty$ are assumed as sound data because the thickness of the specimen used in Section 4 is 20 mm. In the phase images, interior defects are identified as color contrast constructed from distribution of $\Delta\phi(f)$. Therefore, defect detection is easiest when $\Delta\phi$ reaches a maximum ($\Delta\phi_{\max}$), and the frequency at $\Delta\phi_{\max}(f_{\max})$ is defined as the optimum frequency. Figure 3 shows that $\Delta\phi_{\max}$ decreases with decreasing d, and that its decreasing ratio for Sample 2 ($\alpha' = 4.2$) is greater than for Sample 1 ($\alpha' = 1$, isotropic material), which is caused by the larger amount of heat diffusion in the in-plane direction for Sample 2. In contrast, $f_{\max}$ increases concomitantly with decreasing d. The calculated $f_{\max}$ is represented for $d = 10$ mm as a function of defect depth in Fig. 4, where results for $d = \infty$ are also depicted. Because α_T is the same for Samples 1–5, and heat flow is one-dimensional in the case of $d = \infty$, $f_{\max}$ for $d = \infty$ is independent of the samples: $f_{\max}$ for finite size ($d = 10$ mm) defects are larger than those for $d = \infty$ for all hs, and increases with increasing α'.

Figure 5 exhibits $\Delta\phi_{\max}$ for each α' as a function of the defect depth ($d = 10$ mm). This figure shows that $\Delta\phi_{\max}$ significantly decreases with increasing α', and means that defects become more difficult to detect for materials with stronger anisotropy.

In phase images, phase noise appears due to the existence of temperature noise before Fourier transform [19]. The detectable depth of defects by PPT strongly depends on phase noise. A defect is undetectable in PPT when phase noise becomes greater than $\Delta\phi$. Consequently, phase noise is compared with $\Delta\phi_{\max}$ for $\alpha' = 4.2$

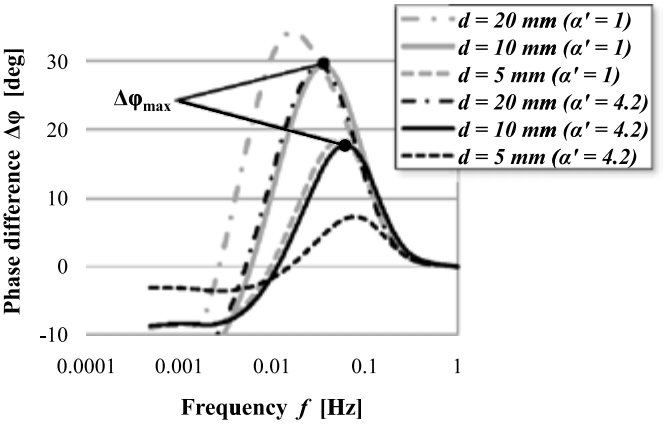

Figure 3. Calculated phase difference as a function of frequency for $d = 5\sim20$ mm for Sample 1 and Sample 2 ($\alpha' = 1$ and 4.2). The phase difference is the difference between at the surface of the sound body ($d = \infty$, $h = 20$ mm) and of a specimen with a finite diameter defect ($h = 1$ mm).

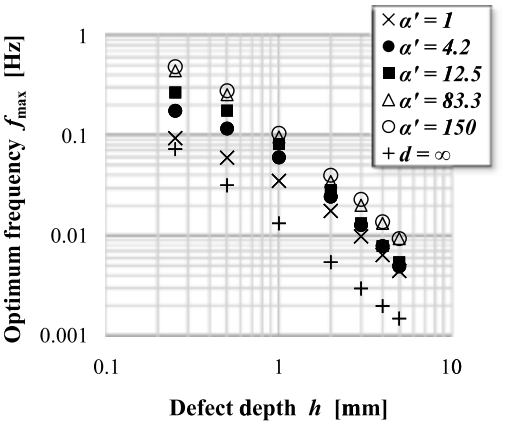

Figure 4. Analytically obtained relation between the optimum frequency $f_{\max}$ and defect depth h for $d = 10$ mm and ∞.

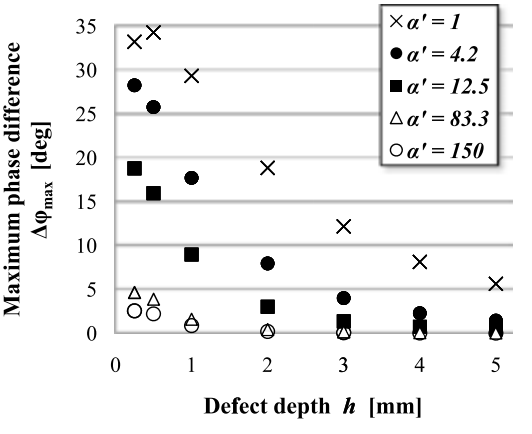

Figure 5. Relation between the maximum phase difference ($\Delta\phi_{\max}$) and defect depth (h) for various α'.

($d = 10$ mm) in Fig. 6. The phase noise in this figure is a peak-to-peak value at each frequency calculated from the temperature noise caused by the infrared camera used in the experiment (see Section 4) [14]. The phase noise decreases with decreasing f, and $\Delta\phi_{\max}$ for $h = 5$ mm is still larger than phase noise. Therefore, it is expected that defects with a depth of less than 5 mm are detectable.

4. Experimental

PPT experiments for CFRP specimens of types were conducted to verify the analytical results presented above.

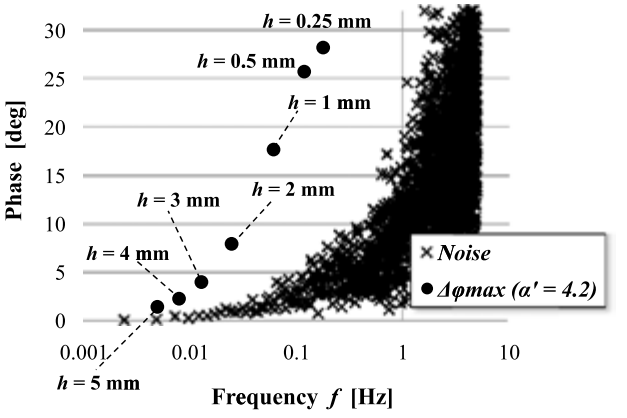

Figure 6. Comparison between maximum phase difference ($\Delta\phi_{\max}$) for each depth of defect (h) with $d = 10$ mm ($\alpha' = 4.2$) and phase noise, which was simulated from temperature noise from an infrared camera used in experiments.

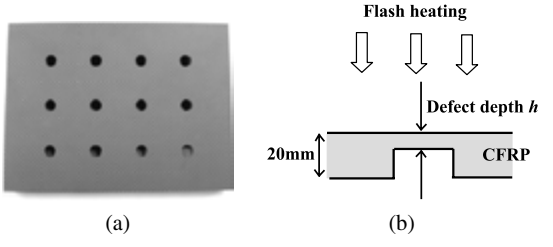

Figure 7. (a) CFRP specimen with flat bottom holes (Specimen A), (b) typical cross-section of the CFRP specimen.

4.1. Experimental Setup

A thermo Inspector (Krautkramer Japan Co. Ltd) [20] was used for experiments. This system consists of flash lamps, an infrared camera (SC4000; FLIR Systems) and a PC used for data processing. For thermal excitation, two Xe flash lamps (each with input energy of 2000 J/F) were used. These lamps have a rectangular flash heating pattern with duration of 3 ms. The infrared camera was equipped with 320 × 256 InSb detectors (detectable wavelength region: 3–5 μm). Its noise-equivalent temperature difference (NETD) was 25 mK. Application software was run on a PC to calculate the phase–frequency relation from temperature–time data obtained using an infrared camera, and to construct phase images.

For experiments, CFRP specimens of two types with different thermal properties (Specimens A and B) were used. An image of Specimen A is shown in Fig. 7(a) along with its cross-sectional drawing in Fig. 7(b). Specimen A is a plain-woven CFRP laminate reinforced with PAN-based fiber (T300; Toray), having a fiber volume fraction of 56%. In contrast, Specimen B is a laminate consisting of uni-directional prepregs reinforced with pitch-based fiber (DIALEAD; Mitsubishi Plastics), having a fiber volume fraction of 55%. The matrix for both specimens is

Table 2.
Two types of CFRP specimens

	Specimen A	Specimen B
Size (mm)	150 × 200 × 20	200 × 200 × 6
Defect diameter d (mm)	10	10
Defect depth h (mm)	0.5∼15	0.2∼4.0
$\alpha'(=\alpha_L/\alpha_T)$	4.2	150

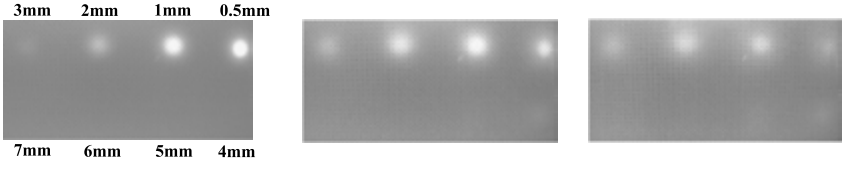

Figure 8. Temperature images for Specimen A ($d = 10$ mm) obtained at (a) 10 s, (b) 20 s and (c) 30 s after flash heating. This figure is published in color in the online version.

epoxy resin. The ratios between the thermal diffusivity in the in-plane direction and that in the out-of-plane direction (α') for Specimens A and B are, respectively, 4.2 and 150 (these are the same values as those for Samples 2 and 5 in Table 1). Flat-bottomed holes of 10 mm diameter were drilled into the non-heated surface of each specimen as artificial defects. The details of the defects are given in Table 2. For the experiments, the temperature distribution on the heated surface was monitored using an infrared camera with sampling frequency of 10 Hz.

4.2. Results

Figures 8 and 9, respectively, show the experimentally obtained temperature and phase images for Specimen A. These images were focused on the defects at 0.5–7 mm depth, and the numerals in Fig. 8(a) and Fig. 9(a) show the defect depth. Figures 8(a)–(c) were observed at 10, 20 and 30 s after flash heating. These images show deeper defects appear with increasing elapsed time. However, the maximum defect depth detected in temperature images was 3 mm (in Fig. 8(b) and (c)), and deeper defects remained undetected even when observed for longer periods. Meanwhile, Fig. 9(a) is the phase image at the optimum frequencies for $h = 5$ mm and $d = 10$ mm obtained from the analytical results (Fig. 4), and similarly with Fig. 9(b) for $h = 4$ mm, Fig. 9(c) for $h = 3$ mm, Fig. 9(d) for $h = 2$ mm and Fig. 9(e) for $h = 1$ mm. These results show that deeper defects appear with decreasing frequency, and the contrast between sound and defective area becomes clearest at the optimum frequency for each depth. Experimentally obtained optimum frequencies (the frequency at which the phase difference reaches maximum) for $l = 0.5$–5 mm are compared with analytical results ($\alpha' = 4.2$) in Fig. 10. Calculated f_{max} values are thoroughly consistent with experimentally obtained results. At the optimum fre-

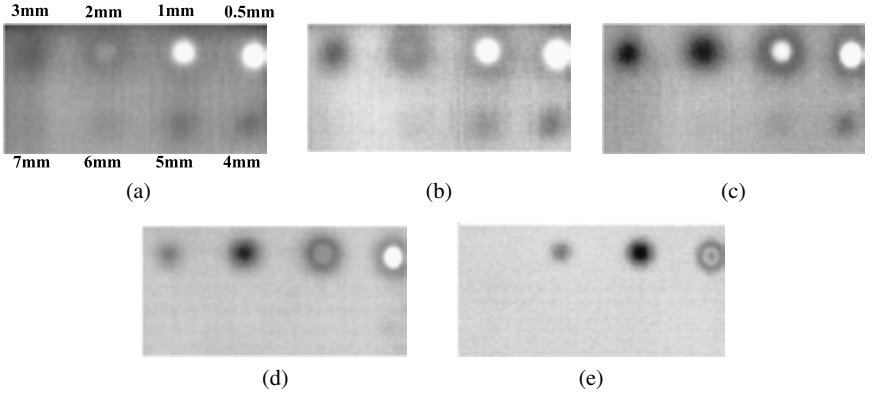

Figure 9. Phase images for Specimen A ($d = 10$ mm) at the optimum frequency of (a) 0.005 Hz, (b) 0.007 Hz, (c) 0.011 Hz, (d) 0.021 Hz and (e) 0.056 Hz. This figure is published in color in the online version.

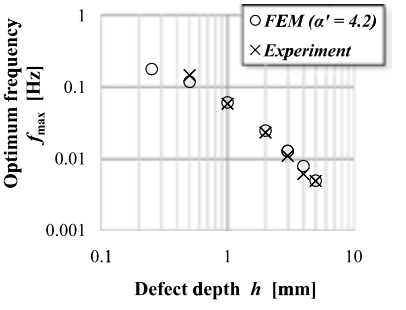

Figure 10. Comparison between the optimum frequencies obtained from FEM analyses ($\alpha' = 4.2$) and from the experiment for Specimen A.

quency, defects lying at 5 mm depth can be detected in the present experiment. This result agrees with the analytical prediction (Fig. 6), and shows the improvement compared with the temperature images. Furthermore, previous papers reported that detectable depth of defects with 10 mm diameter was up to 3 mm by PT [3] or by PPT without consideration of the optimum frequency [17]. Therefore, compared to those results, the detectable defect depth is better in the present results.

Figure 11(a)–(c), respectively, portray phase images for Specimen B observed at the frequencies of 1.0, 0.28 and 0.09 Hz (Fig. 11(b) and (c) are the images at the optimum frequency for $l = 0.5$ and 1 mm). These results demonstrate that phase contrast between sound and defective areas in Specimen B is much smaller than that in Specimen A: this is due to the larger α' of Specimen B (see Fig. 5). Detectable defect depth was up to 1–1.2 mm at 0.09 Hz, and deeper defects remained undetected even when lower frequency was used. In addition, defects in Fig. 11 are observed as elliptical shapes. This phenomenon is caused by the influence of fiber direction in the uppermost layer of the laminate, and obviously demonstrates the influence of high thermal diffusivity in the in-plane direction.

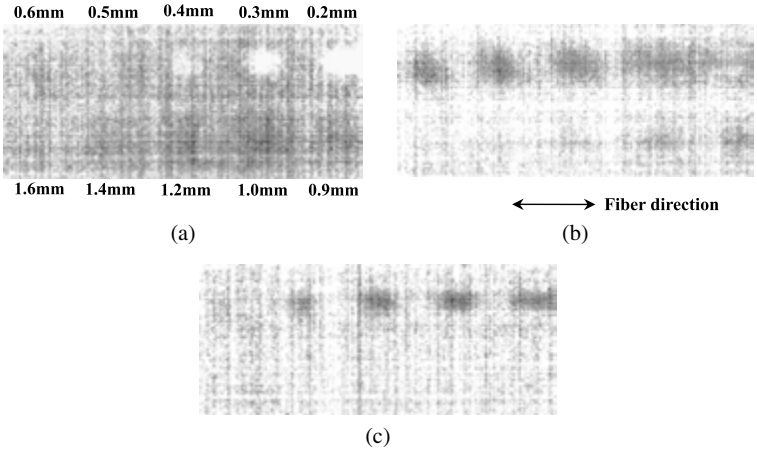

Figure 11. Phase images for Specimen B at the frequency of (a) 0.09 Hz, (b) 0.28 Hz and (c) 1.0 Hz. This figure is published in color in the online version.

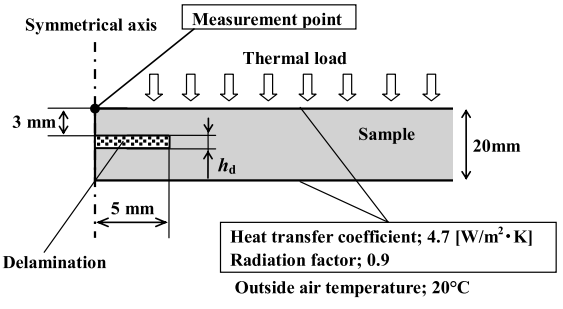

Figure 12. Axisymmetric model with a delamination defect.

5. Discussion for Detecting Delamination Type Defects

In the previous sections, flat-bottomed holes were discussed as artificial defects. However, the most serious defects in CFRPs are of a delamination type. Thus, the phase difference between defective and non-defective areas of the delamination type defects is studied in this section.

Similar to the procedure described in Section 3, FEM analyses were conducted for studying the phase difference on the surface above delamination defects. Figure 12 represents an analytical model used in calculations for the delaminations. In the model, the defect diameter is 10 mm, and defect depth from heating surface is 3 mm. Surface phase differences were obtained for the cases when delamination thicknesses h_d were 0.1 and 0.5 mm. Other analytical conditions (such as boundary conditions) were the same as those described in Section 3.

Figure 13 compares calculated phase differences for two delamination type defects with that for a flat-bottomed hole defect with depth of 3 mm. This figure clearly shows that maximum phase differences for the delamination defects are

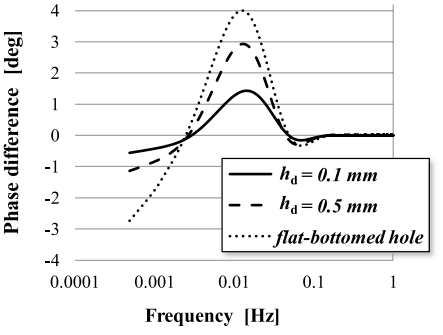

Figure 13. Phase difference between defective and non-defective surface for delamination and flat bottomed-hole shape defect (defect diameter is 10 mm, depth is 3 mm).

smaller than that for the flat-bottomed hole defect, and is decreased with decrease in h_d. Thus, the detectable defect depth for delamination type defects is expected to be smaller than that for flat-bottomed hole defects.

6. Conclusion

Non-destructive testing for CFRPs using pulse phase thermography (PPT) was discussed. The influence of thermal anisotropy on phase data obtained using the PPT was studied analytically. Experiments for two CFRP specimens with different anisotropy were performed. The obtained findings are as follows:

1. The optimum frequencies for detection of defects at various depths increase concomitantly with the increase in the ratio of thermal diffusivities in the in-plane direction to that in the through-thickness direction (α').
2. The phase difference between the defective area and the sound area decreases significantly for the materials with stronger anisotropy.
3. Defects with 10 mm in diameter were detectable up to depth of 5 mm in the CFRP reinforced with PAN-based fiber (having lower α') by considering optimum frequency. In contrast, it was up to only 1 mm in the CFRP unidirectionally reinforced with pitch-based fiber having much larger α'.

References

1. S. Sugimoto, T. Ogasawara, Y. Aoki and T. Ishikawa, Damage detection of composites using pulsed thermography, in: *Proc. 15th Intl Conf. Compos. Mater. — ICCM-15*, Durban, South Africa (2005).
2. N. P. Avdelidis, B. C. Hawtin and D. P. Almond, Transient thermography in the assessment of defects of aircraft composites, *NDT&E Int.* **36**, 433–439 (2003).
3. T. Krell, R. Brandenburg and E. Lauterborn, Comparative investigation of pulse thermography and shearographic testing of composite materials, in: *Proc. 9th Eur. Conf. NDT — ECNDT*, Berlin, Germany (2006).

4. S. Pickering and D. Almond, Matched excitation energy comparison of the pulse and lock-in thermography NDE techniques, *NDT&E Int.* **41**, 501–509 (2008).
5. G. Busse, Nondestructive evaluation of polymer materials, *NDT&E Int.* **27**, 253–262 (1994).
6. D. Wu and G. Busse, Lock-in thermography for nondestructive evaluation of materials, *Rev. Gen. Therm.* **37**, 693–703 (1998).
7. Th. Zweschper, A. Dillenz, G. Riegert, D. Scherling and G. Busse, Lockin thermography methods for the NDT of CFRP aircraft components, in: *Proc. 8th Eur. Conf. NDT — ECNDT*, Barcelona, Spain (2002).
8. W. Bai and B. S. Wong, Evaluation of defects in composite plates under convective environments using lock-in thermography, *Meas. Sci. Technol.* **12**, 142–150 (2001).
9. G. Busse, D. Wu and W. Karpen, Thermal wave imaging with phase sensitive modulated thermography, *J. Appl. Phys.* **71**, 3962–3965 (1992).
10. X. Maldague and S. Marinetti, Pulse phase infrared thermography, *J. Appl. Phys.* **79**, 2694–2698 (1996).
11. R. Monranini, Quantitative determination of subsurface defects in a reference specimen made of Plexiglas by means of lock-in and pulse phase infrared thermography, *Infrared Phys. Technol.* **53**, 363–371 (2010).
12. C. Ibarra-Castanedo and X. Maldague, Defect depth retrieval from pulsed phase thermographic data on plexiglas and aluminum samples, *Proc. SPIE* **5405**, 348–356 (2004).
13. F. Weritz, R. Arndt, M. Rollig, C. Maierhofer and H. Wiggenhauser, Investigation of concrete structures with pulse phase thermography, *Mater. Struct.* **38**, 843–849 (2005).
14. M. Ishikawa, H. Hatta, Y. Habuka, S. Jinnai and S. Utsunomiya, Pulse phase thermography for detection of deeper defects, *NDT&E Int.* (submitted).
15. C. Ibarra-Castanedo and X. Maldague, Pulse phase thermography inversion procedure using normalized parameters to account for defect size variation, *Proc. SPIE* **5782**, 334–341 (2005).
16. S. Marinetti, Y. A. Plotnikov, W. P. Winfree and A. Braggiotti, Pulse phase thermography for defect detection and visualization, *Proc. SPIE* **3586**, 230–238 (1999).
17. P. Servais, Development of a new NDT method using thermography for composite inspection on aircraft with portable military thermal imager, in: *Proc. 9th Eur. Conf. NDT — ECNDT*, Berlin, Germany (2006).
18. S. Jinnai, Y. Nishitani, Y. Habuka and M. Ishikawa, Application of active thermography — near surface detect performance of pulse thermography test method, in: *Proc. 12th Sympos. Surface Methods, Japanese Soc. Non-Destruct. Inspect.*, pp. 52–57 (2009).
19. X. Maldague, Y. Largouet and J. P. Couturier, A study of defect depth using neural networks in pulsed phase thermography: modeling, noise, experiments, *Rev. Gen. Therm.* **37**, 704–717 (1998).
20. Krautkramer Japan, http://www.krautkramer.co.jp/products/thermo_inspector/index.html.